Microstructure and Mechanical Properties of 17-4 PH Stainless Steel Fabricated by Gas Metal Wire Arc Additive Manufacturing

Javad Mohammadi [a], Iman Dashtgerd [b], Sola An [b], Billythong Trinh [b], Amir Mostafaei [b,*], A.Reza Riahi [a,*]

[a] Department of Mechanical, Automotive, and Materials Engineering, University of Windsor, Windsor, Ontario N9B 3P4, Canada

[b] Department of Mechanical, Materials, and Aerospace Engineering, Illinois Institute of Technology, Chicago, IL 60616, USA

* corresponding authors: mostafaei@iit.edu (A. Mostafaei), ariahi@uwindsor.ca (A.R. Riahi)

Abstract

Wire arc additive manufacturing (WAAM) presents a highly promising alternative to conventional subtractive manufacturing methods to produce metallic components, particularly in the aerospace industry, where there is a demand for 17-4 precipitation-hardened (PH) stainless steel structures. This study focuses on investigating the microstructural characteristics, showing microhardness evaluations, and analyzing the tensile properties of the as-printed parts during the 17-4 PH manufacturing process at different locations and directions. The fabrication is carried out using gas metal wire arc additive manufacturing (GM-WAAM). As a result, it was found that the microstructure of the as-deposited part showed a complex configuration consisting of both finely equiaxed and coarsely formed δ-ferrite phases with vermicular and lathy morphologies. These phases were dispersed inside the martensitic matrix, while a small amount of retained austenite was also present. It was observed that the volume fraction of retained austenite (20% to 5%) and δ-ferrite phases (15.5% to 2.5%) decreased gradually from the bottom to the top of the as-deposited wall. This reduction in the fractions of these phases resulted in a progressive increase in both hardness (~37%) and ultimate tensile strength (UTS) along the building direction. This study successfully fabricates a high-strength and ductile 17-4 PH as-printed part using WAAM. The findings provide evidence supporting the feasibility of employing WAAM for producing defect-free, high-strength components on a large scale while maintaining mechanical properties similar or better than wrought alloy 17-4 PH.

Keywords: Wire arc additive manufacturing; 17–4PH Stainless Steel; Microstructure analysis; Mechanical properties.

1. Introduction

Over the past 30 years, additive manufacturing (AM) technology has undergone consistent development, creating new processes that allow for the design and manufacture of components with intricate internal structures [1-4]. AM systems can be classified into different categories based on the type of material feedstock usage. The three main classifications are powder bed, powder feed, and wire feed systems [5-7]. Wire arc additive manufacturing (WAAM) is a highly advanced and efficient fabrication process in the field of AM process. WAAM enables the production of large metallic parts with minimal material waste, making it a cost-effective and time-efficient solution [8]. WAAM offers enhanced design flexibility and customization options, allowing for the creation of near-net-shape components of varying complexities [9, 10]. Among other AM techniques, WAAM stands out with its excellent deposition rate, often reaching several ($Kg.h^{-1}$). This remarkable rate is achieved through high feedstock usage efficiency, making WAAM a distinct and advantageous choice for rapid and efficient part production [11-13]. WAAM has been successfully utilized for the manufacturing of a various range of metallic materials. This includes the use of gas metal arc welding (GMAW) [14], gas tungsten arc welding (GTAW) [15], and plasma arc welding (PAW) methods [16]. These welding techniques have been effectively employed in WAAM to deposit and shape various metallic materials, such as Ti-6Al-4V [17], aluminum [16], steel [18, 19], and nickel [20].

The precipitation-hardening (PH) stainless steels (SS), such as 17-4 PH, 15-5 PH, and 13-8 PH are good candidates for AM process due to their excellent weldability. They are used in various applications due to their high strength, ductility, and corrosion resistance. They are commonly used in various industries, including aerospace, pressure vessels, petrochemical, and food processing components. The high strength of PH alloys creates challenges when using conventional manufacturing techniques. Consequently, AM can be considered a promising solution for producing near-net-shape components of PH alloys in a single-step process [21, 22]. During the solidification process of PH alloys, they initially form δ-ferrite and subsequently undergo a transformation into austenite as the cooling takes place. Finally, at room temperature, the austenite transforms into martensite. The resulting martensitic structure in PH alloys is comparatively finer and softer when compared to other martensitic stainless steels. This can be attributed to the low carbon content typically found in PH alloys, which is commonly less than

0.05 wt% [23]. The strength of PH alloys increased s through ageing, which involves forming small homogeneous precipitation phases within the martensitic matrix [24-26].

Welding of 17-4 PH presents challenges due to various types of cracking, such as cold cracking [27], solidification cracking [28], reheat cracking [29], and hydrogen-induced cracking (HIC) [30]. Additionally, there is a potential for the formation of delta ferrite during the welding of martensitic steel [31]. According to Ghaffari et al. [32], the presence of δ-ferrite in PH 13-8Mo can significantly impact its tensile and hardness properties. They found that the hardness increased gradually from the first layer to the last layer, which correlated with a decrease in δ-ferrite content from 13% to 2%. The formation of δ-ferrite has a detrimental effect on other mechanical properties, such as creep resistance and ductility. The formation of δ-ferrite in weld metal is influenced by the cooling rate, as discussed by Sam et al. [33]. They found that there is a critical cooling rate, theoretically dependent on the composition of the feedstock material and above the critical cooling rate, where the formation of δ-ferrite becomes more likely. They indicated that controlling the cooling rate is a crucial factor in managing the formation of δ-ferrite and its potential impact on the microstructure and mechanical properties of the weld [34]. Arivazhagan et al. [34] demonstrated that reducing the heat input during welding decreases δ-ferrite formation, as it enhances the cooling rate. In a recent investigation, Roy et al. [35] found that eliminating of δ-ferrite in AM martensitic stainless steel can lead to a remarkable reduction of over 70% in the scatter of tensile data and an increase of 20% in yield strength.

There is currently a lack of research on the application of WAAM for 17-4 PH. The previous studies on AM of 17-4 PH mainly focused on laser-based processes with powder materials. These studies focus on the detailed analysis of the microstructure and mechanical properties of 17-4 PH produced through Laser powder bed fusion (L-PBF) processes. These investigations aimed to comprehensively understand the material's behavior, including its microstructural features and mechanical performance, to optimize the L-PBF parameters and enhance the quality of the fabricated components [36, 37]. Yadollahi et al. [38] took an additional step in mechanically characterizing of 17-4 PH fabricated part with L-PBF. They investigated the impact of building orientation and post-fabrication heat treatment on fatigue behavior. The study discovered that horizontally built specimens exhibited a greater fatigue strength attributed to the orientation of deposited layers and defects in relation to the loading axis. Caballero et al. [21] studied the effect of shielding gas, scanning strategy, and post-heat treatment on the mechanical

properties of 17-4 PH fabricated by WAAM. Although the assessment of microstructure characterization was limited, they were successful in achieving high deposition rates for 17-4 PH stainless steel as one of the tested materials.

In this study, additive manufacturing technology was employed to fabricate wire-arc 17-4 PH. The aim was to examine the relationship between microstructural variations along the building direction and the resulting anisotropic mechanical behavior of the deposited wall. The mechanical properties of the deposited walls were evaluated through microhardness and uniaxial tensile tests. Additionally, fractography analysis was conducted on the fractured surfaces of the tensile specimens. It was anticipated that the mechanical properties of the deposited walls would be equal to or higher than those of the wrought alloy at room temperature. This expectation was based on the understanding that the thermal history during manufacturing influenced the formation of microconstituents in the microstructure.

2. Experimental Procedure

2.1. Materials and Manufacturing Process

In this study, wire arc additive manufactured walls were fabricated with approximate dimensions of 120 × 70 × 18 mm. The walls were constructed by depositing 40 consecutive layers using a commercially available ER630 (AWS A5.9) welding wire with a diameter of 0.9 mm (0.035 in). The chemical composition of the welding wire is listed in Table 1. To carry out the AM process, an Everlast power supply, the MTS 251 SI model GMAW machine equipped with a cold metal transfer (CMT) mode and a torch path on a three-axis CNC machine, was utilized as the heat source. Process parameters were optimized to ensure a defect-free wall by depositing several trial layers on a 6 mm thick ASTM A693 Grade 630 hot rolled plate. The optimized parameters were provided in Table 2. A pure shielding gas consisting of 99.99% argon (Ar) was used to protect the melt pools from oxidation and environmental contaminants. The shielding gas was supplied at a flow rate of 20 L.min^{-1}. Throughout the WAAM process, the wire extension was consistently maintained at 12.7 mm. For the fabrication of the multi-layer wall, parallel paths were followed to simulate the deposition direction of adjacent layers. To ensure proper layer adhesion, an inter-pass temperature of 150 ± 10 ºC was maintained between the deposition of successive layers. This temperature was carefully measured and controlled using a digital non-contact infrared thermometer.

Table 1. Chemical compositions (wt.%) of filler metal and substrate

Element	C	Cr	Ni	Mo	Nb	Mn	Si	P	S	Cu	Fe
ER 630	0.03	16.50	4.80	0.21	0.22	0.54	0.43	0.02	0.02	3.64	Bal.
A 639 Gr 630	0.03	16.22	4.85	0.25	0.20	0.48	0.51	0.03	0.05	3.82	Bal.

Table 2. Used processing parameters for the WAAM of 17-4 PH.

Arc Current (A)	Arc Voltage (V)	Wire Feed Speed mm.s^{-1}	Travel Speed mm.s^{-1}	Shielding Gas L.min^{-1}
140 ± 10	19.5 ± 1	85	6	18-20

2.2. Microstructural Characterization

The samples were cut along the building direction into dimensions of 10 mm × 10 mm × 15 mm, to examine the microstructure of the specimens, as shown in s **Error! Reference source not found.**(a) and 1(b). The cut surfaces of the samples were mounted with epoxy resin, ground with sandpapers up to 4000 grits, and polished using 3, 1, and 0.05 μm diamond paste solution. The sample surfaces were sonicated in ethanol for 5 minutes to avoid the presence of impurities, followed by chemical etching. The etching solution used consisted of a mixture of 4g copper sulphate, 20 mL of hydrochloric acid, and 20 mL of water. This etching process revealed the microstructural features of the samples. Microstructural analysis was carried out using advanced imaging techniques. The Keyence laser scanning microscope (VK-X100) and the scanning electron microscope (SEM) model FEI Quanta 200 Environmental SEM equipped with an EDAX Octane Plus SDD Detector were employed. The Keyence laser scanning microscope provided high-resolution microstructure images, while the SEM allowed for more detailed investigation and analysis. An X-ray diffraction machine, specifically the ARL XTRA X-ray diffractometer model, was employed for phase analysis, utilizing Cu-Kα radiation at an accelerative voltage and current of 35 kV and 30 mA, respectively. The 2θ range covered 20-100° with a scan rate of 1 s/step and a scan step size of 0.02°. The XRD data collected was subjected to analysis using MAUD software to extract crystallographic parameters. A JEOL 5900LV scanning electron microscope (SEM) with an integrated electron backscattered diffraction (EBSD) system by Oxford Instruments was employed for examination. Data acquisition was conducted using AzTec software, utilizing

operational settings with an accelerating voltage of 20 keV and a step size of 0.5 μm. Post-processing of the initial EBSD data was executed using the HKL Channel 5 software package. Furthermore, MTEX, a toolbox based on MATLAB, was utilized for additional analysis [39].

2.3. Hardness and Tensile Tests

Microhardness tests were conducted on the samples using a Buhler micro-Vickers hardness tester, following the ASTM-E384 standard [39]. A diamond indenter was utilized with a load of 1 kg and a dwell time of 10 seconds. Microhardness measurements were performed in the direction of the building process, and a minimum of 800 measurements were taken from the samples' bottom, middle, and top regions to ensure statistical validity. The deposited walls were cut in horizontal and vertical directions to prepare flat tensile specimens, as illustrated in **Error! Reference source not found.**(b). Tensile tests were conducted at room temperature using a universal testing machine (MTS 50KN). Following the tensile tests, the fracture surfaces of the specimens were examined using a scanning electron microscope (SEM) to study the fracture characteristics and gain further insights into the failure mechanisms.
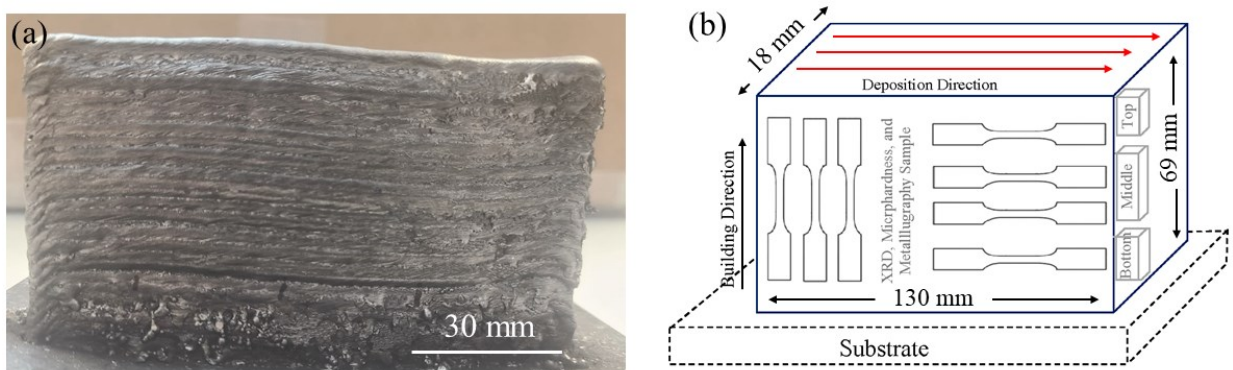

Figure 1 . (a) As printed WAAM 17-4 PH sample, (b) location, direction for microstructural analysis and tensile tests relative to building and deposition directions.

3. Results and Discussion

3.1. Microstructural analysis

Error! Reference source not found. presents optical microscopy images illustrating the microstructural characteristics observed in the building direction. Columnar grain structures are typically observed in both regions along the building direction, characterized by the presence of inter-dendritic δ-ferrite within the coarse martensitic structure. However, due to the rapid cooling

rate and non-equilibrium conditions inherent to the WAAM process, the transformation of δ-ferrite to austenite is hindered. As a result, a considerable portion of the δ-ferrite phase remains untransformed, while most of the austenite obtained transforms to martensite. This observation is consistent with findings from previous literature [32, 40-42].

Consequently, the material's microstructure contains a notable quantity of δ-ferrite embedded within the martensite phase at room temperature. Recent studies on WAAM of 17-4 PH have also reported a similar microstructure [43, 44]. The remaining morphology and orientation of the δ-ferrite phases show variations between the columns of the original δ-ferrite grains. These δ-ferrite phases can be observed in two primary morphologies: lathy and vermicular shapes (as shown in **Error! Reference source not found.** (a) and (b)). It was previously hypothesized that these distinct ferrite morphologies were a result of local fluctuations in composition and variations in cooling conditions within the material. The morphology of the δ-ferrite is influenced by three key factors: (1) the alloy composition, specifically the Cr/Ni equivalent ratio; (2) the cooling rate during the AM process; and (3) the crystal orientation between the δ-ferrite and austenite phases.
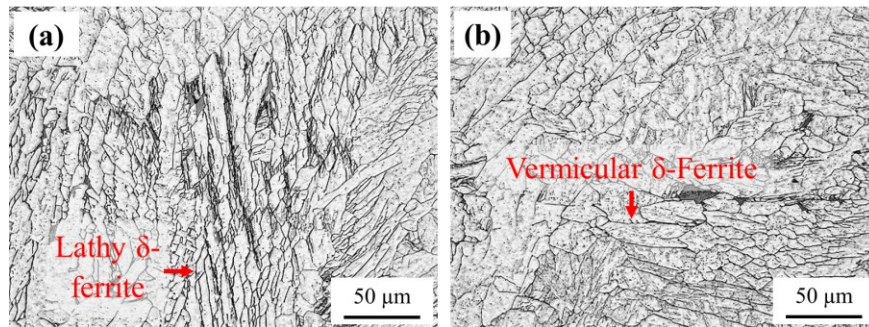
Figure 2. Optical microscopy images of the as-built microstructure parallel to the building direction (a) columnar structure and (b) polygonal structure.

Increasing the Cr/Ni ratio has resulted in higher overall δ-ferrite content, including an increase in lathy δ-ferrite [45, 46]. However, the rapid cooling rate associated with the AM process inhibits the complete transformation of δ-ferrite to austenite. The transformation relies on solid-state diffusion, which is limited by the fast-cooling nature of AM. This phenomenon is not exclusive to AM, as high cooling rates during laser welding have also been reported to impede the transformation of δ-ferrite to austenite. [47-49].

Figure 3 presents SEM images taken from different regions of as-deposited walls, namely the bottom, middle, and top portions. The wall primarily consists of fine martensite laths initiated

by austenite transformation. The fine martensite laths grow in the same direction as the primary austenite grain. The cooling rate strongly influences the proportion of residual δ-ferrite during the solidification of AM process. Higher cooling rates tend to reduce the diffusional transformation of δ-ferrite to austenite, leading to a higher volume fraction of δ-ferrite remaining at room temperature. In contrast, the utilization of slower cooling rates provides sufficient time for the diffusional transformation to reach the end. Consequently, this leads to a reduction in the proportion or quantity of δ-ferrite that remains in the solidified deposit part at room temperature [50, 51]. In Figure 3(a) andFigure *3*(b), a continuous network of the lathy δ-ferrite phase is evident. However, the microstructure of the top region (Figure 3c) exhibits noticeable differences compared to the bottom and middle regions. The top section contains a significant volume of vermicular-shaped δ-ferrite. This distinct phase forms along the primary austenite grain boundaries and is embedded within a martensitic matrix.
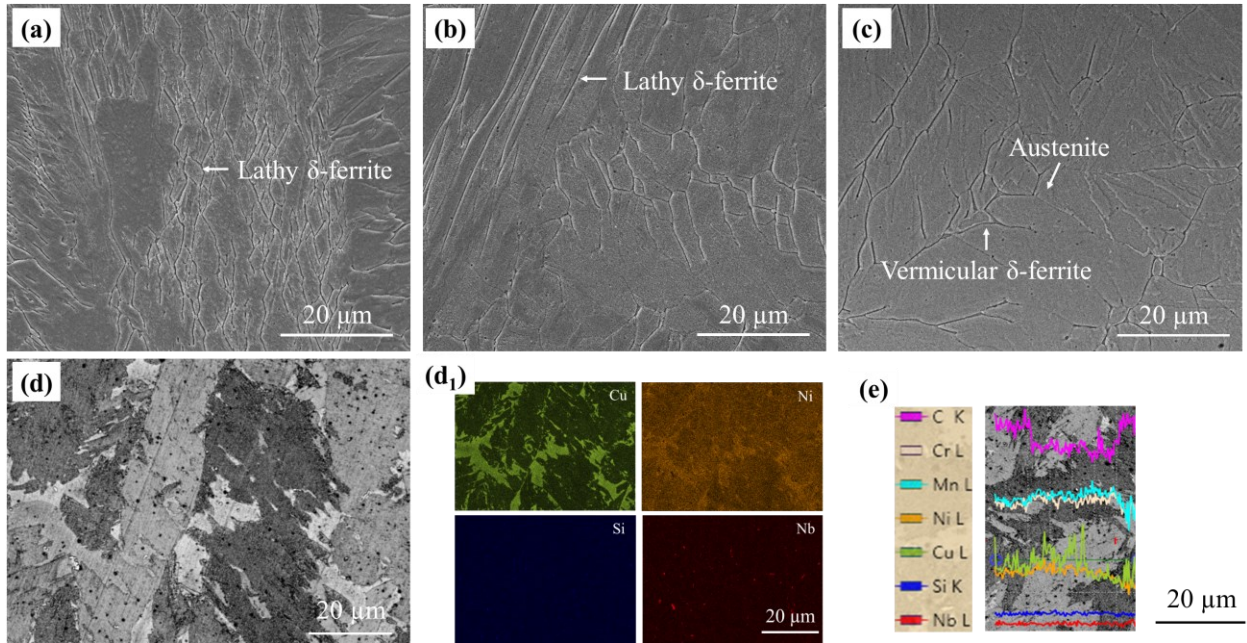

Figure 3. SEM images comparing the fraction of δ-ferrite formed in the as built condition (a) bottom, (b) middle, and (c) top regions of the deposited wall. (d) SEM micrograph and (d₁) EDS elemental concentration maps and (e) line scans taken from the as-deposited microstructure of WAAM 17-4PH.

The cooling rate exhibits variation from the bottom to the top regions of the material due to several factors. These factors include (1) the influence of the substrate acting as a heat sink. The substrate absorbs and dissipates heat from the material, facilitating faster cooling in the regions in

direct contact with it. This heat sink effect plays a crucial role in determining the cooling rate in the bottom regions of the material, (2) the application of an interpass temperature around 150 ± 10 °C further contributes to the variation in cooling rates within the material. This temperature range is carefully maintained between consecutive deposition passes throughout the AM process. Its primary purpose is to manage the heat input and effectively control the cooling rate, consequently exerting an influence on the thermal behavior and the development of its microstructure and (3) heat accumulation within the part during the fabrication process is another factor that influences the variation in cooling rates. As the AM process advances, heat generated from each successive deposition pass accumulates within the material. This accumulated heat changes the local temperature distribution and affects the cooling rate in different regions. Consequently, the level of heat accumulation within the part plays a significant role in determining the overall thermal behavior and can result in differing cooling rates throughout the material. However, as the fabrication process advances, heat transfer becomes increasingly dominated by conduction through the accumulated heat from previously deposited layers. This dominance of conduction results in a gradual decrease in the cooling rate from the bottom to the top of the component. As a result, the volume fraction of δ-ferrite in the top regions (2.5%) is substantially lower compared to the middle (9.7%) and bottom (15.5%) sections of the wall, as shown in Figure 3.

The concentration maps obtained from Energy Dispersive Spectroscopy (EDS) analysis, taken from the microstructure in the middle region of the as-deposited part as shown in Figure 3(d), have confirmed the locations of the retained austenite phase within the inter-dendritic regions. These regions present higher concentrations of Cu and Ni elements, which are known as austenite stabilizing elements [52]. Additionally, analysis of the line scan using EDS and the Cu concentration map in Figure 3(e) have revealed the presence of spherical inclusion particles distributed randomly in the microstructure. These particles are primarily composed of Si and Nb. The formation of Nb-rich and Si-rich oxides revealed the presence of oxygen in the shielding gas and possible moisture on the surface of the feedstock material.

When a new layer is deposited, it has two outcomes. Firstly, it generates heat that impacts the underlying layers, resulting in higher temperatures for the closer layers in comparison to the preceding layers. This, in turn, leads to the creation of a heat-affected zone (HAZ) characterized by a martensite microstructure. The nearby layers can reach temperatures at which austenitization occurs, causing a partial or localized transformation of their martensite matrix into austenite. As

the material cools down, this austenite is partially retained within the martensitic matrix. Secondly, the elevated temperatures associated with depositing the new layer disrupt the continuous network of the δ-ferrite phase in the bottom and middle areas. In HAZ regions, the δ-ferrite phases undergo a retransformation into austenite, which subsequently shifts to martensite during the cooling process (see **Error! Reference source not found.**).
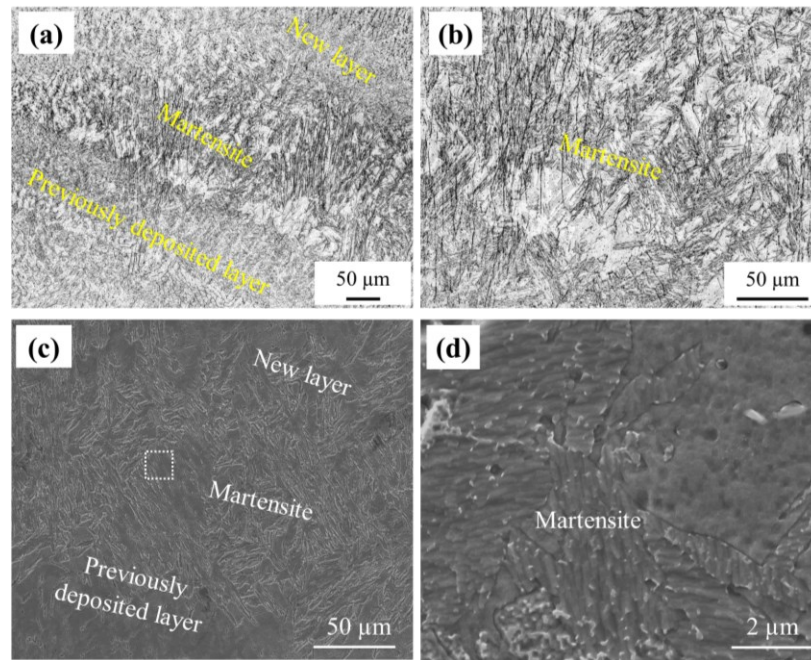

Figure 4. (a, b) optical microscopy, and (c, d) high magnification SEM micrographs of the HAZ between two subsequent deposited layers.

EBSD measurements were conducted on the as-deposited 17–4 PH part manufactured through the WAAM process to understand the crystallographic orientation further and enhance the precision of phase identification. **Error! Reference source not found.**(a-c) displays fine martensite laths, each exhibiting nearly identical orientations within every primary columnar grain. In the high-magnification band contrast map with overlaid lath boundary misorientations, the misorientations of the laths are predominantly marked by a dense population of low-angle grain boundaries ranging from 2° to 15°. The martensitic laths exhibit elongation at an inclined angle rather than aligning along the building direction, possibly influenced by the disruption of the deposition direction. With a minimum misorientation angle of 10.53° between martensitic blocks, also referred to as martensitic variants [53], these blocks are separated by high-angle grain boundaries over 10°. In the AM process of 17–4PH, the shift from prior austenite to martensitic

variants is influenced by a combined orientation relationship involving both Kurdjumov-Sachs (K-S) and Nishiyama-Wasserman (N-W) mechanisms [54]. This suggests a notable dislocation density within the as-printed sample. The deposition process leads to the generation of a high density of dislocations, primarily attributed to the occurrence of martensitic transformation. In **Error! Reference source not found.**(d)-5(f), the inverse pole figure (IPF) phase maps illustrate that the matrix exhibits a body-centered cubic (bcc) crystallographic structure (depicted by the blue region). This structure represents both the residual δ-ferrite and the lath martensitic structure, while the SEM micrographs did not reveal the formation of retained austenite. The IPF phase map in **Error! Reference source not found.**(d) indicated the existence of small grains exhibiting a face-centered cubic (fcc) structure (depicted by the red regions). This observation confirms the formation of a low volume fraction of retained austenite (2.35%) within the as-printed structure. The presence of retained austenite is attributed to the inclusion of 8 wt% Ni in the feedstock material, which stabilizes austenite.
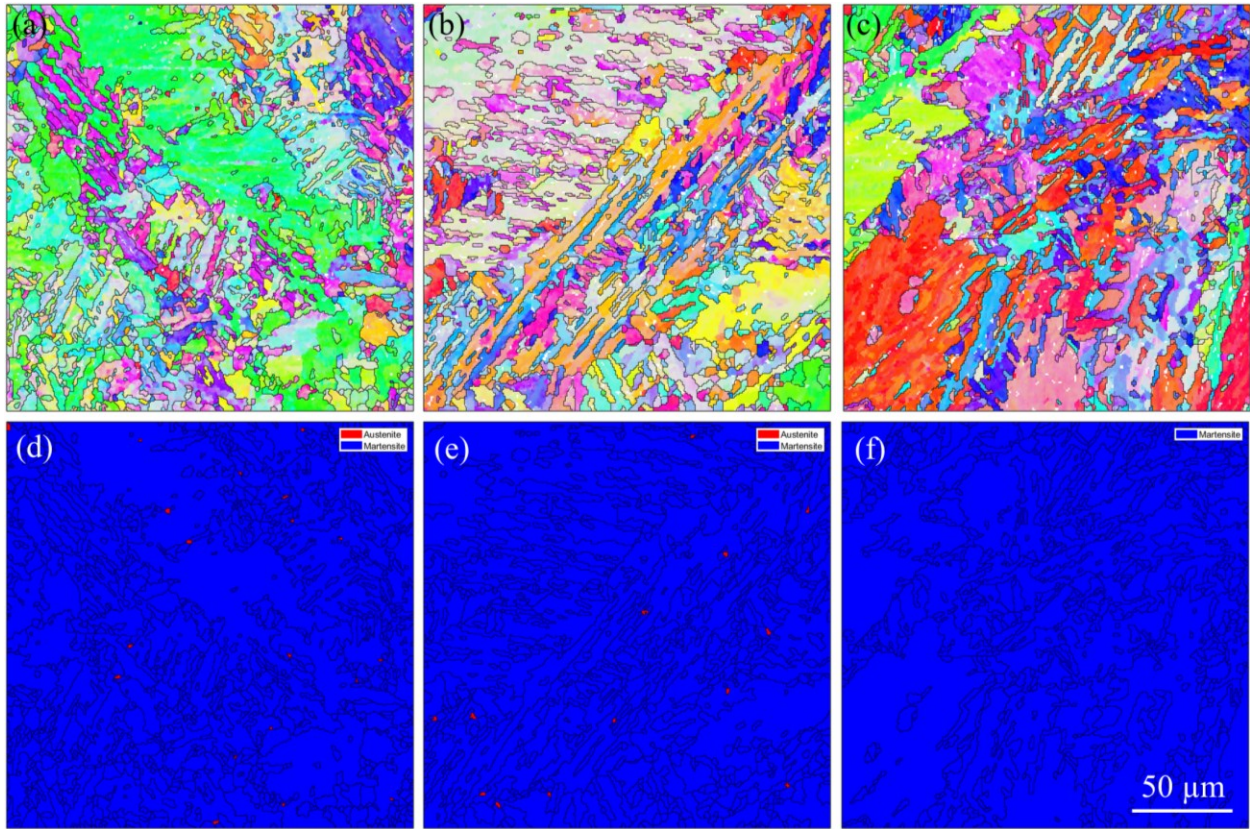

Figure 5. EBSD micrographs and IPF maps taken from the (a,d) bottom, (b,e) middle, and (c,f) top regions of the as-deposited WAAM 17-4 PH.

Additionally, the complex thermal history experienced during the AM process, involving sequential heating and cooling cycles, contributes to the formation of retained austenite. This in-situ thermal treatment closely resembles the quenching and separating heat treatment, a process designed to enhance the proportion of retained austenite in martensitic steels [55]. This research maintains a consistent interpass temperature throughout the WAAM process, ensuring uniform cooling rates in both the upper and lower layers. Consequently, it is estimated that there will be a similar proportion of retained austenite in both these regions. **Error! Reference source not found.**(d-f) show a notably increased proportion of austenite in the bottom region in contrast to the top region of the sample. This observation implies the potential occurrence of reversed austenite formation in the bottom part of the as-deposited wall. The microstructure of each deposited layer is expected to consist of a combination of δ-ferrite, martensite, and retained austenite at the inter-pass temperature (i.e. 150 ± 10 ºC).

The following deposition of layers raises the temperature of the previous layer beyond the martensite start temperature (Ms) and generates enough driving force to obtain carbon atoms from the martensite. These carbon atoms then diffuse into the austenite, which, characterized by a face-centered cubic (fcc) crystal structure, exhibits significantly higher carbon solubility [56]. The higher concentration of carbon, acting as an austenite stabilizing element, reduces both the (Ms) and (Mf) temperature and leads to a higher formation of retained austenite at room temperature [57].

3.2. XRD Analysis

X-ray diffraction (XRD) analysis was shown on the as deposited sample taken from three distinct sections of the as-printed part, covering from the bottom to the top of the wall. The findings of this analysis are presented in Figure 6(a). The primary objective of this analysis was to compare the volume fraction of retained austenite at different locations within the deposited wall, specifically at the bottom, middle, and top regions (see Figure 6(b)). In all the examined regions, characteristic peaks corresponding to both bcc (martensite and δ-ferrite) and fcc (retained austenite) phases were identified. A decreasing trend in the content of retained austenite was observed along the building direction. The percentages of retained austenite were approximately 22% at the bottom, 18% in the middle, and 5% at the top regions of the deposited wall.

The differences observed in the volume fraction of retained austenite can be attributed to the varying multiple cooling and heating cycles in AM [52, 58, 59]. Multiple cooling and heating cycles have a notable influence on the distribution of retained austenite. In the initial layers (also known as the first layers), the rapid cooling rate induced by the solid and cool substrate, possessing enhanced heat dissipation capabilities, led to the formation of a higher proportion of retained austenite. Additionally, the materials deposited on the top layer remained unaffected by thermal cycling, resulting in the lowest retained austenite content compared to the middle layers.
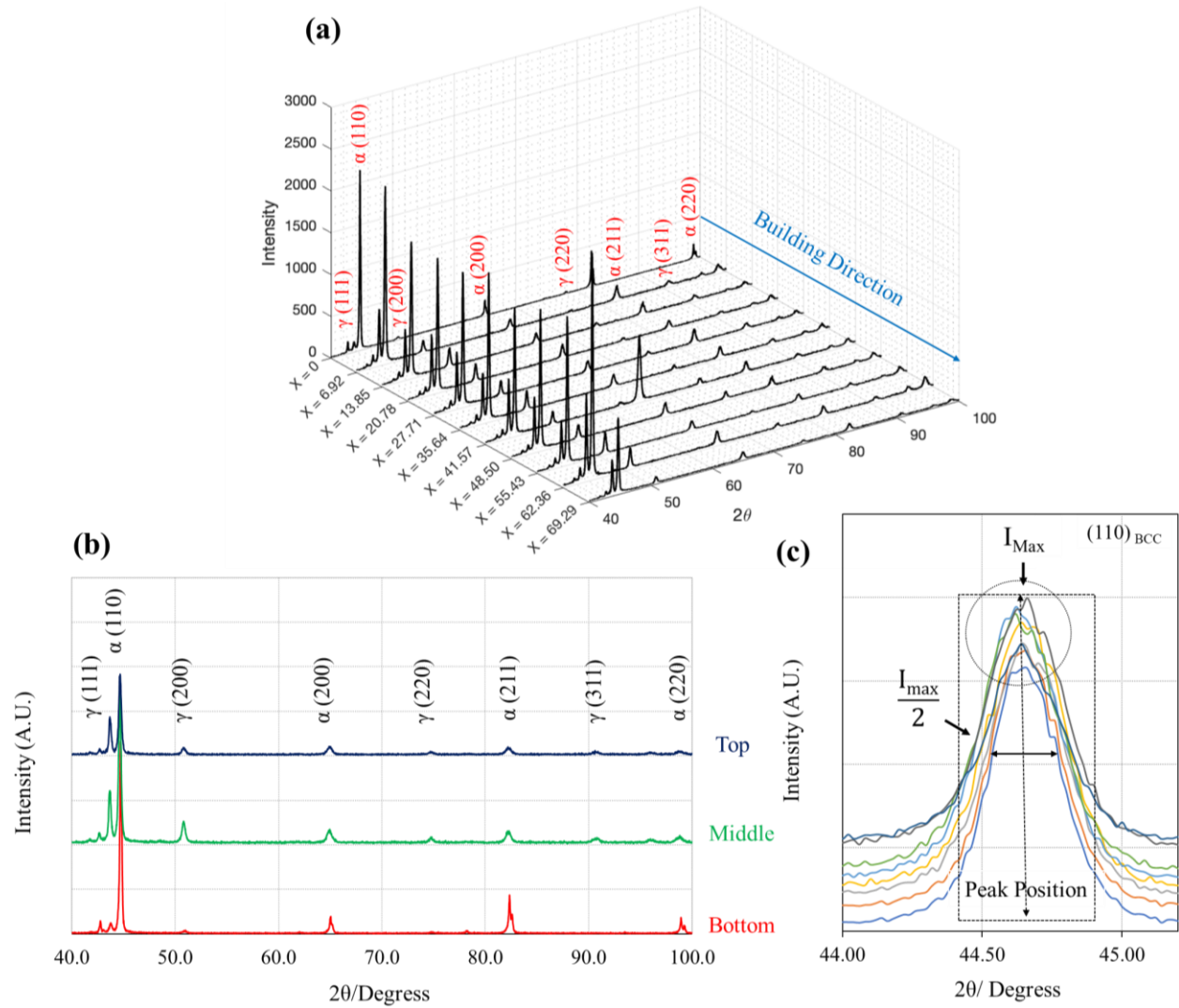

Figure 6. The X-ray diffraction patterns were obtained: (a) building direction from bottom to top surface, (b) individual bottom, middle, and top regions of the as deposited 17-4 PH wall, and (c) FWHM of each diffraction peak at $(110)_{BCC}$.

The width of the XRD peak in different regions was analyzed by measuring the full width at half maximum (FWHM) of each diffraction peak in the as-deposited sample in Figure 6(c). provides a schematic representation of the measurement process, and the resulting values are summarized in Table 3. The average FWHM values showed a minor increase from the bottom to the top regions of the as-deposited sample. This increase is closely associated with the elastic lattice strain and dislocation density present in the sample [60, 61]. The phenomenon can be attributed to solid-state transformations of nitrogen and carbon atoms happening inside the martensite matrix during the multiple cooling and heating cycles employed in the WAAM process. Thus, the microstructural characterization results indicate that the WAAM of the 17-4 PH component shows a dominant microstructure primarily of vermicular and lathy residue δ-ferrite. Additionally, there is a minor presence of retained austenite dispersed within a finely structured martensitic matrix. An interesting finding is the gradual reduction in both the volume fraction of δ-ferrite and retained austenite from the bottom to the top of the deposited wall. This observation suggests that the morphology of the δ-ferrite is influenced by the differing thermal conditions, such as specific temperature profiles and cooling rates experienced by the layers as they are built up in the building direction.

Table 3. The full width at half maximum (FWHM) of the XRD peaks for the as-deposited 17-4 PH.

Plane (hkl)	Bottom		Middle		Top	
	2θ	FWHM	2θ	FWHM	2θ	FWHM
(110) BCC	44.72	0.221	44.64	0.276	44.68	0.297
(200) BCC	65.06	0.292	64.96	0.642	64.88	0.615
(211) BCC	82.34	0.528	82.30	0.655	82.12	0.635
(220) BCC	98.92	0.739	98.80	0.862	98.90	0.688

3.3. Mechanical properties

3.3.1. Vickers microhardness Measurement

Figure 7 shows hardness maps obtained from three distinct positions along the vertical axis of the as-deposited part. These maps include 800-850 indents, with intervals of 300 μm between each point from the bottom to the top in the building direction. In Figure 7 (a), the base material and bottom regions ASTM A639 Gr 630 are represented by a solid blue-, yellow-, and orange-colored regions, respectively. The saturated blue, yellow, and orange colors indicate hardness values exceeding 330 ± 10 HV$_1$. Moving to the middle part demonstrates a stable trend in hardness

values in the building direction. Also, the softer regions corresponding to individual and parallel welded beads can be distinguished by their green color. The hardness map of the middle region shows a consistent level of homogeneity, with an average value of 327 ± 15 HV$_1$. This homogeneity can be attributed to the occurrence of quasi-steady state heat flow during the manufacturing process, where the heat input and dissipation reach a relatively stable state. The quasi-steady state conditions contribute to the uniform hardness distribution observed in the middle region [62], providing insights into the structural integrity and mechanical properties of the build. The region labeled as top represents the uppermost layers of the structure. Towards the lower section, there exists a region with a hardness value of 340 ± 10 HV$_1$, which aligns with the hardness values observed in most parts of the structure. However, approaching the final layers, there is a transition to approximately 350 ± 5 HV$_1$. Additionally, these last layers show significant discontinuities indicated by exceptionally low hardness points.

The hardness map clearly indicates a gradual upward trend in hardness value as it moves towards the upper sections of the deposited wall, with a substantial increase observed in the top layers (as shown in Figure 7(b)). The minimum hardness value recorded in the bottom regions was 277 HV$_1$, while the maximum value in the upper layers reached 380 HV$_1$, indicating an approximate 37% increase in hardness value in the building direction. Increasing hardness values in the building direction resulted in the reducing of the volume fraction of residual δ-ferrite, and the content of retained austenite. Moreover, the materials deposited on the top layer did not undergo thermal cycling and hence also maintained fine-grained structures. The highest Vickers microhardness values were associated with the less stress-relieved δ-ferrite phases at the top layers. Similar behavior was also reported in WAAM of 13-8 PH [32, 41].
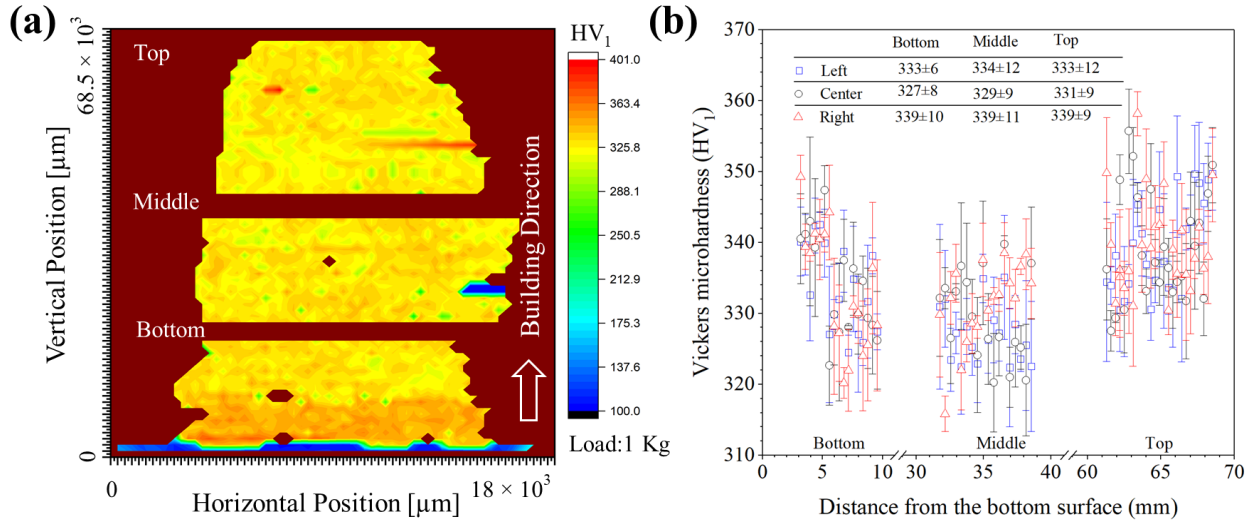
Figure 7. (a) Vickers microhardness map from different locations in the sample height including top, middle, and bottom layers. These images display the hardness variations along the building direction. (b) The plot shows a three-stage rise in hardness based on the distance from the bottom surface to the top of the deposited wall. Error bars represent the standard deviation from the average value in three distinguishing dot layers.

3.3.2. Tensile strength

Figure 8(a) shows the engineering stress-strain curves of the as-deposited 17-4 PH for both horizontal and vertical directions. The average ultimate tensile strength (UTS) for the horizontal samples (1165 ± 22 MPa) was found to be similar to that of the vertical samples (1169 ± 18 MPa). However, a significant difference in elongation percentage was observed between the two directions. The horizontal direction demonstrates a substantially higher elongation percentage of 12.5±3.8% compared to the vertical direction, which only reaches 7.2±1.3%. This discrepancy suggests that printed samples exhibited significantly greater ductility during the deposition process than in the building direction. Anisotropic mechanical properties, particularly in terms of ductility, are frequently observed in AM parts. This phenomenon has been extensively documented in prior studies across a range of metals and alloys used in AM, such as stainless steel and steel [63, 64]. The anisotropy in the ductility of the 17-4 PH as deposited part can be explained by two microstructural imperfections identified in this study. These imperfections include the formation of a restricted number of primary δ-ferrite grain boundaries in the building direction (as shown in Figure 8(b)), which can result in reduced ductility. The presence of these grain boundaries can create preferential paths for crack propagation and limit the material's ability to deform uniformly as well as the formation of localized brittle zones in the HAZ [65, 66]. The HAZ experiences rapid

heating and cooling during the fabrication process, leading to the formation of brittle martensite and austenite phases. These localized brittle areas exhibit lower ductility compared to the surrounding material, consequently affecting the overall ductility in the vertical direction.

Although there are similarities in the average tensile test results between the two directions, individual samples exhibited variations in yield and tensile strength. This indicates that the tensile strength of the 17-4 PH processed through WAAM did not display significant anisotropy. This behavior can be attributed to the similar microstructure in both the vertical and horizontal directions within each deposited specimen. In this study, the WAAM process demonstrated an impressive average UTS of (1166 ± 22) MPa for 17-4 PH material. This UTS value is notably greater than the UTS values listed in

Table *4* for the 17-4 PH parts produced via the AM technique. The anisotropic behavior observed in the WAAM 17-4 PH can be attributed to the formation of a columnar primary δ-ferrite grain structure during the solidification process of deposited parts. This leads to a preferential texture along the building direction, as confirmed by the results of the SEM and EBSD analysis shown in Figure 3 and Figure 5.
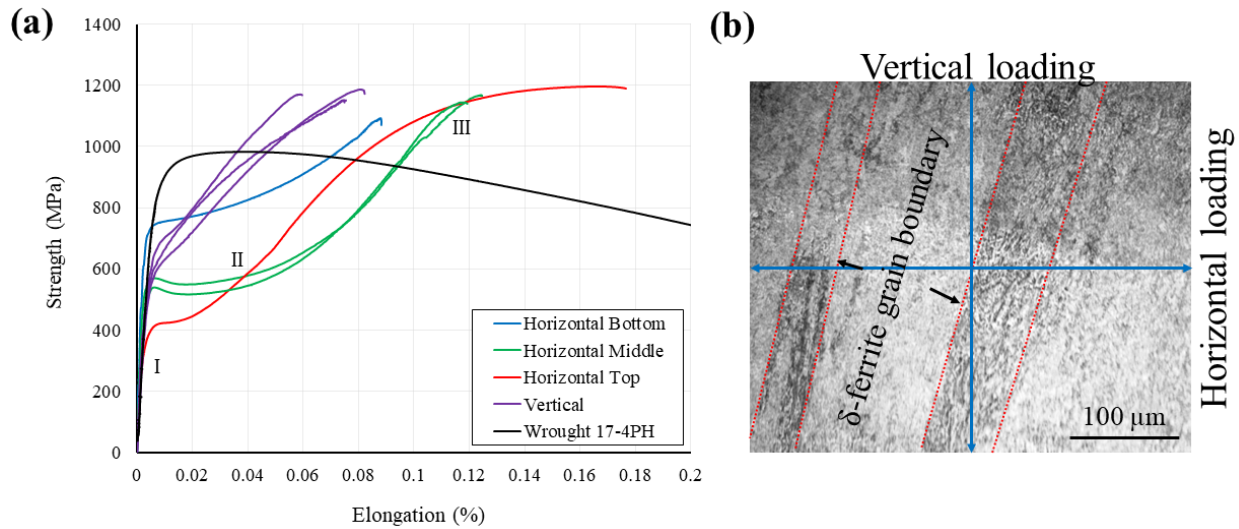

Figure 8. (a) stress-strain curves of the as-printed wall in the vertical and horizontal directions, and (b) the relative orientation between the tensile loading direction and primary columnar crystals.

Reducing the amount of δ-ferrite can have a positive impact on the strength, ductility, and elongation properties of the deposited parts. δ-ferrite phases are known to be relatively softer and less ductile compared to austenite and martensite. Therefore, minimizing the presence of δ-ferrite in the building direction makes the as deposited parts less prone to localized deformation and

failure, in which leads to improved elongation behavior, as illustrated in Figure 8a. Additionally, the overall strength of the as-deposited part in the building direction is increased. In the horizontal direction of the as deposited samples, both the upper and lower yield points were observed in Figure 8(a) (areas II and III). This behavior (elastic lattice strain) can be attributed to the presence of a high density of dislocations and the interaction of interstitial elements, such as carbon (C), nitrogen (N), and oxygen (O), with the dislocation fields during the process of plastic deformation. Nitrogen acts as a strong austenite stabilizer, contributing to the stability of the austenite phase and the formation of retained austenite within the matrix upon cooling [67]. Interstitial elements, such as carbon and nitrogen, diffuse and attach themselves to dislocations when plastic deformation occurs during the upper yield point, in which nitrogen is more efficient than carbon due to its higher solubility and diffusion coefficient. When dislocations are released from the interstitial atoms, slip can occur at a reduced stress level at a lower yield point. Consequently, the dislocations that have been released are able to move at a lower stress level [68, 69]. The increase in the elongation in the yielding observed from stage II, characterized by the lower yield point and uniform elongation, to stage III, as indicated by the green and red curves in Figure 8a can be attributed to the presence of a high density of dislocations and the transformation of austenite to martensite during plastic deformation.

Table 4. Average values of yield strength (YS), ultimate tensile strength (UTS), and elongation (EL) results for samples tested in the horizontal and vertical directions.

AM processed parts		YS (MPa)	UTS (MPa)	EL (%)	Ref.
WAAM – 17-4 PH As deposited Sample	H	650±14	1165±15	12.5±3.8	This study
	V	691±7	1169 ± 18	7.2±1.3	
WAAM of 17-4 PH	H	842±65	1009±55	12.2±0.7	[21]
	V	738±30	979±13	11.6±0.3	
	H	678±3	975±16	11.7±0.1	[44]
	V	---	---	---	
Wrought ASTM A693 Grade 630		≥ 954	≥ 725	≥ 20	This study

Indeed, the application of a solutionizing and aging heat treatment can significantly enhance UTS and hardness values of the as-deposited 17-4PH alloy. This process led to the formation of finely distributed Cu precipitates inside tempered martensite [70]. The homogenous

distribution of Cu precipitates contributes to the desired improvements in the 17-4PH mechanical properties, which is the subject of the authors' upcoming study.

3.3.3. Fractography

The analysis of the fracture surfaces resulting from the tensile test, as illustrated in Figure 9, reveals the influence of microstructural variations on the mechanical performance of the as-deposited part. These fracture surfaces provide valuable evidence regarding the plastic deformation that occurred during the tensile testing of the specimens. The horizontal samples showed a range of conical and cup-shaped dimples, indicating that the formation and merging of small micro-voids primarily influenced the fracture mechanism. Furthermore, some areas' fracture morphology displays characteristics associated with the δ-ferrite phase. Ductile samples showed a higher concentration of dimples in the central region of the fracture surface, while the edges of the fracture surface, which experienced greater shear loading, revealed shallower dimples known as parabolic dimples with river-like cleavage fracture. In the horizontal samples with higher elongation percentages can be attributed to the superior work hardening behavior, which is mainly influenced by cross-slip mechanisms. These mechanisms contribute to an increased dislocation density, thereby enhancing the ductility of the samples. Similar behavior was also reported in the super solidus liquid phase sintering (SLPS) of 316 stainless steel [71]. The vertical samples showed a less pronounced degree of plastic deformation compared to the horizontal samples and dimples on the fractured surface of the vertical samples have different morphology. This suggests a transition in the failure mechanism towards quasi-cleavage modes in which a combination of ductile (γ-FCC) and brittle (α-BCC and martensite) phases during the tensile testing. The quasi-cleavage fracture surfaces were visible at the center, where pores that facilitated the initiation and propagation of cracks were also observed.
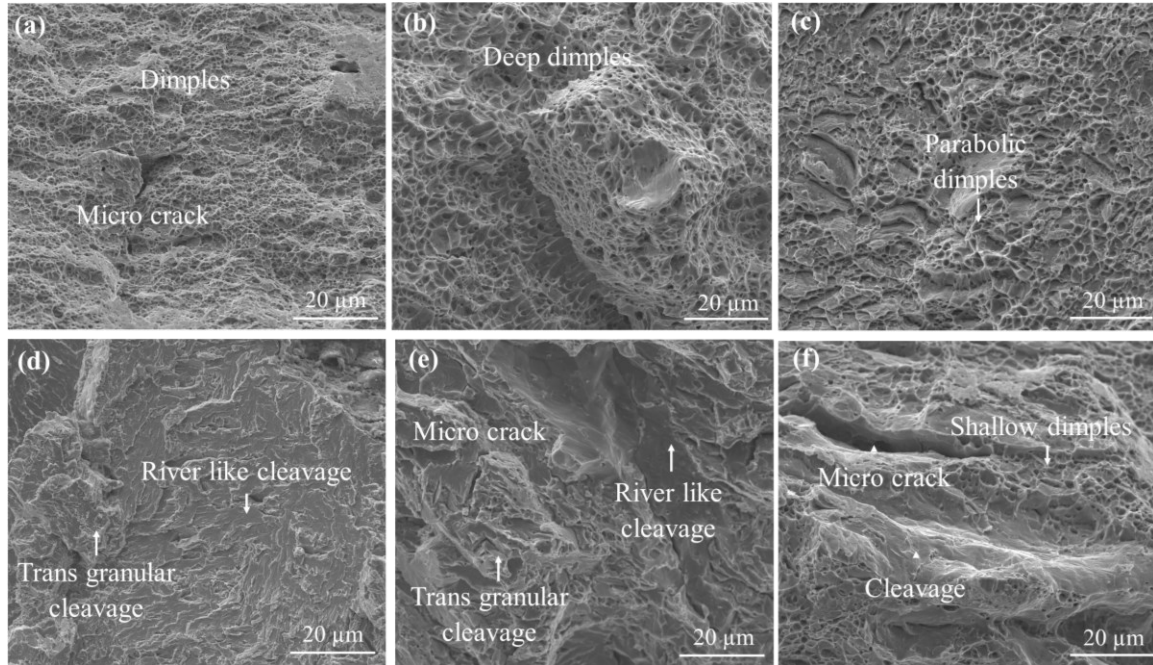
Figure 9. SEM micrographs from the fractured surfaces after tensile testing along (a, b, c) horizontal and (b, d, e) vertical directions.

Detailed analysis of the fractured surfaces (Figure 10) provided further insight into the presence of small spherical inclusions within the dimples and micro-voids. EDS analysis confirmed that these inclusions were primarily composed of higher concentrations of copper (Cu), silicon (Si), and oxygen (O), while exhibiting lower levels of iron (Fe), chromium (Cr), and nickel (Ni). The as-printed structure of the fabricated part also exhibited the presence of Nb-rich oxide and Si- rich oxide inclusions Figure 3(d) to Figure *3*(i). These inclusions play a crucial role as nucleation sites for the formation of micro-voids during the application of tensile load.
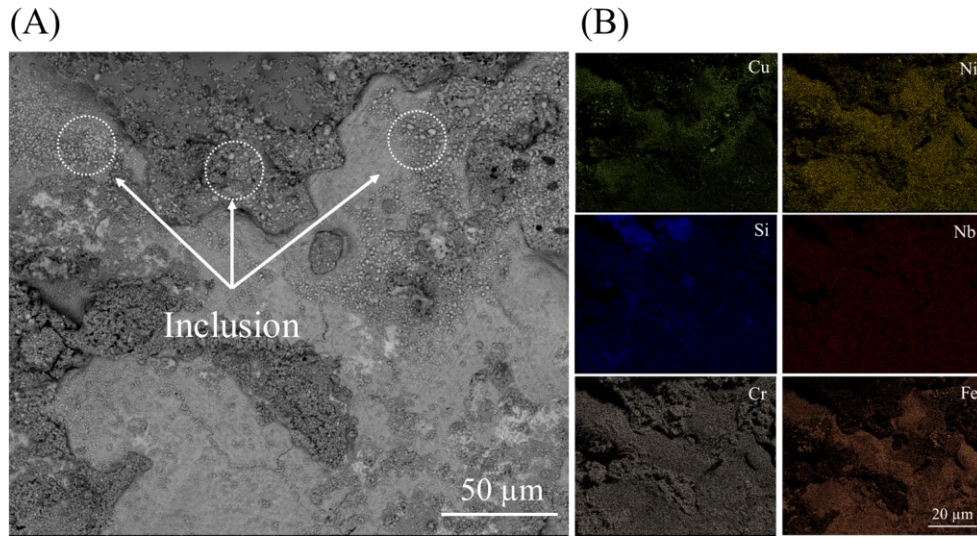
Figure 10. (A) SEM micrograph from the fractured surface and (B) EDS elemental maps showing distribution of elements and presence of inclusions.

4. Conclusion

In this study, a comprehensive analysis was conducted on the microstructural characteristics, microhardness, uniaxial tensile properties, and fractography of a defect-free 17-4 PH sample fabricated using wire arc additive manufacturing (WAAM). The following conclusions were drawn from this investigation:

1. The microstructure of the as-deposited part consisted of a finely equiaxed and coarsely δ-ferrite phase, exhibiting vermicular and lathy morphologies. These structures were distributed within a martensitic matrix, accompanied by a minor volume fraction of retained austenite.

2. The complex thermal cycling during the WAAM process resulted in the formation of heterogeneous microstructural features along the vertical direction. Furthermore, the fraction of retained austenite (22%-5%) and δ-ferrite phases (15.5% to 2.5%) decreased progressively from the bottom to the top of the deposited wall.

3. The as deposited part indicated a gradual increase in hardness and ultimate tensile strength (UTS) in the building direction. This improvement is a result of the lower volume fraction of retained austenite and δ-ferrite in the top regions of the component. Also, microhardness measurements performed on top layers (380 HV_1) revealed a 37% higher value than in the middle and bottom regions (277 HV_1).

4. The tensile strength value 1170±5 of the as-printed part was found to be consistent in both the building and deposition directions. However, significant anisotropy was observed in the

ductility of the as-deposited samples, with approximately double the ductility along the deposition direction compared to the building direction. The fracture surface revealed a characteristic dimple morphology, with more prominent and pronounced dimples observed in the horizontal samples, suggesting greater ductility in that direction.

References

[1] W. E. Frazier, "Metal additive manufacturing: a review," *Journal of Materials Engineering and Performance,* vol. 23, no. 6, pp. 1917-1928, 2014, doi: https://doi.org/10.1007/s11665-014-0958-z.

[2] V. A. Hosseini, M. Högström, K. Hurtig, M. A. V. Bermejo, L.-E. Stridh, and L. Karlsson, "Wire-arc additive manufacturing of a duplex stainless steel: thermal cycle analysis and microstructure characterization," *Welding in the World,* vol. 63, no. 4, pp. 975-987, 2019, doi: https://doi.org/10.1007/s40194-019-00735-y.

[3] J. Lin *et al.*, "Microstructural evolution and mechanical properties of Ti-6Al-4V wall deposited by pulsed plasma arc additive manufacturing," *Materials & Design,* vol. 102, pp. 30-40, 2016, doi: https://doi.org/10.1016/j.matdes.2016.04.018.

[4] O. Yilmaz and A. A. Ugla, "Microstructure characterization of SS308LSi components manufactured by GTAW-based additive manufacturing: shaped metal deposition using pulsed current arc," *The International Journal of Advanced Manufacturing Technology,* vol. 89, no. 1-4, pp. 13-25, 2017, doi: https://doi.org/10.1007/s00170-016-9053-y.

[5] P. Almeida and S. Williams, "Innovative process model of Ti-6Al-4V additive layer manufacturing using cold metal transfer (CMT)," in *2010 International Solid Freeform Fabrication Symposium*, 2010: University of Texas at Austin, doi: http://dx.doi.org/10.26153/tsw/15162.

[6] B. Kianian, "Wohlers Report 2017: 3D Printing and Additive Manufacturing State of the Industry, Annual Worldwide Progress Report: Chapters titles: The Middle East, and other countries," 2017.

[7] B. Wu *et al.*, "A review of the wire arc additive manufacturing of metals: properties, defects and quality improvement," *Journal of Manufacturing Processes,* vol. 35, pp. 127-139, 2018, doi: https://doi.org/10.1016/j.jmapro.2018.08.001.

[8] X. Lu, Y. Zhou, X. Xing, L. Shao, Q. Yang, and S. Gao, "Open-source wire and arc additive manufacturing system: formability, microstructures, and mechanical properties," *The International Journal of Advanced Manufacturing Technology,* vol. 93, no. 5-8, pp. 2145-2154, 2017, doi: https://doi.org/10.1007/s00170-017-0636-z.

[9] Z. Wu *et al.*, "Study of printability and porosity formation in laser powder bed fusion built hydride-dehydride (HDH) Ti-6Al-4V," *Additive Manufacturing,* vol. 47, p. 102323, 2021, doi: https://doi.org/10.1016/j.addma.2021.102323.

[10] S. W. Williams, F. Martina, A. C. Addison, J. Ding, G. Pardal, and P. Colegrove, "Wire+ arc additive manufacturing," *Materials Science and Technology,* vol. 32, no. 7, pp. 641-647, 2016, doi: https://doi.org/10.1179/1743284715Y.0000000073.

[11] B. Shassere, A. Nycz, M. W. Noakes, C. Masuo, and N. Sridharan, "Correlation of microstructure and mechanical properties of metal big area additive manufacturing," *Applied Sciences,* vol. 9, no. 4, p. 787, 2019, doi: https://doi.org/10.3390/app9040787.

[12] N. Rodriguez, L. Vázquez, I. Huarte, E. Arruti, I. Tabernero, and P. Alvarez, "Wire and arc additive manufacturing: a comparison between CMT and TopTIG processes applied to stainless steel," *Welding in the World,* vol. 62, no. 5, pp. 1083-1096, 2018, doi: https://doi.org/10.3390/app10051563.

[13] I. Gibson, D. W. Rosen, and B. Stucker, "Additive manufacturing technologies," vol. 17, 2014, doi: https://doi.org/10.1007/978-3-030-56127-7.

[14] K. Derekar, "A review of wire arc additive manufacturing and advances in wire arc additive manufacturing of aluminium," *Materials science and technology,* vol. 34, no. 8, pp. 895-916, 2018, doi: https://doi.org/10.1080/02670836.2018.1455012.

[15] Y. Xie *et al.*, "Anisotropy of fatigue crack growth in wire arc additive manufactured Ti-6Al-4V," *Materials Science and Engineering: A,* vol. 709, pp. 265-269, 2018, doi: https://doi.org/10.1016/j.msea.2017.10.064.

[16] Y. Luo, J. Li, J. Xu, L. Zhu, J. Han, and C. Zhang, "Influence of pulsed arc on the metal droplet deposited by projected transfer mode in wire-arc additive manufacturing," *Journal of Materials Processing Technology,* vol. 259, pp. 353-360, 2018, doi: https://doi.org/10.1016/j.jmatprotec.2018.04.047.

[17] Q. Wu *et al.*, "Obtaining uniform deposition with variable wire feeding direction during wire-feed additive manufacturing," *Materials and Manufacturing Processes,* vol. 32, no. 16, pp. 1881-1886, 2017, doi: https://doi.org/10.1080/10426914.2017.1364860.

[18] X. Xu, S. Ganguly, J. Ding, S. Guo, S. Williams, and F. Martina, "Microstructural evolution and mechanical properties of maraging steel produced by wire+ arc additive manufacture process," *Materials Characterization,* vol. 143, pp. 152-162, 2018, doi: https://doi.org/10.1016/j.matchar.2017.12.002.

[19] J. Mohammadi, I. Dashtgerd, A. R. Riahi, and A. Mostafaei, "Pulsed gas metal arc additive manufacturing of low-carbon steel: Microstructure observations and mechanical properties," *Materials Today Communications,* vol. 38, p. 107637, 2024, doi: https://doi.org/10.1016/j.mtcomm.2023.107637.

[20] X. Xu, S. Ganguly, J. Ding, C. E. Seow, and S. Williams, "Enhancing mechanical properties of wire+ arc additively manufactured INCONEL 718 superalloy through in-process thermomechanical processing," *Materials & Design,* vol. 160, pp. 1042-1051, 2018, doi: https://doi.org/10.1016/j.matdes.2018.10.038.

[21]   A. Caballero, J. Ding, S. Ganguly, and S. Williams, "Wire+ Arc Additive Manufacture of 17-4 PH stainless steel: Effect of different processing conditions on microstructure, hardness, and tensile strength," *Journal of Materials Processing Technology,* vol. 268, pp. 54-62, 2019, doi: https://doi.org/10.1016/j.jmatprotec.2019.01.007.

[22]   L. Zai *et al.*, "Laser powder bed fusion of precipitation-hardened martensitic stainless steels: a review," *Metals,* vol. 10, no. 2, p. 255, 2020, doi: https://doi.org/10.3390/met10020255.

[23]   R. J. Hamlin and J. N. DuPont, "Microstructural evolution and mechanical properties of simulated heat-affected zones in cast precipitation-hardened stainless steels 17-4 and 13-8+ Mo," *Metallurgical and Materials Transactions A,* vol. 48, pp. 246-264, 2017, doi: https://doi.org/10.1007/s11661-016-3851-6.

[24]   G. Yang, F. Deng, S. Zhou, B. Wu, L. Qin, and J. Zheng, "Influence of shielding gas nitrogen content on the microstructure and mechanical properties of Cu-reinforced maraging steel fabricated by wire arc additive manufacturing," *Materials Science and Engineering: A,*   vol.   832,   p.   142463,   2022,   doi: https://doi.org/10.1016/j.msea.2021.142463.

[25]   A. Ladewig, G. Schlick, M. Fisser, V. Schulze, and U. Glatzel, "Influence of the shielding gas flow on the removal of process by-products in the selective laser melting process," *Additive   Manufacturing,*   vol.   10,   pp.   1-9,   2016,   doi: https://doi.org/10.1016/j.addma.2016.01.004.

[26]   I. Jurić, I. Garašić, M. Bušić, and Z. Kožuh, "Influence of Shielding Gas Composition on Structure and Mechanical Properties of Wire and Arc Additive Manufactured Inconel 625," *JOM,* vol. 71, no. 2, pp. 703-708, 2019, doi: https://doi.org/10.1007/s11837-018-3151-2.

[27]   V. J. Badheka, S. Agrawal, and N. Shroff, "Mode of Failure of Resistance Spot Welded Martenstic Stainless Steel-Part II," *International Journal of Mechanical and Materials Engineering,* vol. 5, no. 1, pp. 43-52, 2010.

[28]   L. Aucott *et al.*, "Initiation and growth kinetics of solidification cracking during welding of steel,"   *Scientific   reports,*   vol.   7,   no.   1,   p.   40255,   2017,   doi: https://doi.org/10.1038/srep40255.

[29]   A. Dhooge and A. Vinckier, "Reheat cracking—A review of recent studies," *International Journal of Pressure Vessels and Piping,* vol. 27, no. 4, pp. 239-269, 1987, doi: https://doi.org/10.1016/0308-0161(87)90012-3.

[30]   J. C. Lippold and D. J. Kotecki, *Welding metallurgy and weldability of stainless steels*. 2005.

[31]   D. Carrouge, H. Bhadeshia, and P. Woollin, "Microstructural change in high temperature heat-affected zone of low carbon weldable'13% Cr' martensitic stainless steels," *Stainless Steel World(The Netherlands),* vol. 14, pp. 16-17, 2002, doi: https://citeseerx.ist.psu.edu/.

[32]   M. Ghaffari, A. V. Nemani, and A. Nasiri, "Microstructure and mechanical behavior of PH 13–8Mo martensitic stainless steel fabricated by wire arc additive manufacturing," *Additive Manufacturing,*   vol.   49,   p.   102374,   2022,   doi: https://doi.org/10.1016/j.addma.2021.102374.

[33]   S. Sam *et al.*, "Delta ferrite in the weld metal of reduced activation ferritic martensitic steel," *Journal of Nuclear Materials,* vol. 455, no. 1-3, pp. 343-348, 2014, doi: https://doi.org/10.1016/j.jnucmat.2014.07.008.

[34]   B. Arivazhagan, G. Srinivasan, S. Albert, and A. Bhaduri, "A study on influence of heat input variation on microstructure of reduced activation ferritic martensitic steel weld metal produced by GTAW process," *Fusion Engineering and Design,* vol. 86, no. 2-3, pp. 192-197, 2011, doi: https://doi.org/10.1016/j.fusengdes.2010.12.035.

[35]   S. Roy *et al.*, "Mitigating Scatter in Mechanical Properties in AISI 410 Fabricated via Arc-Based Additive Manufacturing Process," *Materials,* vol. 13, no. 21, p. 4855, 2020, doi: https://doi.org/10.3390/ma13214855.

[36]   M. Mahmoudi, A. Elwany, A. Yadollahi, S. M. Thompson, L. Bian, and N. Shamsaei, "Mechanical properties and microstructural characterization of selective laser melted 17-4 PH stainless steel," *Rapid Prototyping Journal,* 2017, doi: https://doi.org/10.1108/RPJ-12-2015-0192.

[37]   A. Mostafaei *et al.*, "Defects and anomalies in powder bed fusion metal additive manufacturing," *Current Opinion in Solid State and Materials Science,* vol. 26, no. 2, p. 100974, 2022, doi: https://doi.org/10.1016/j.cossms.2021.100974.

[38]   A. Yadollahi and N. Shamsaei, "Additive manufacturing of fatigue resistant materials: Challenges and opportunities," *International Journal of Fatigue,* vol. 98, pp. 14-31, 2017, doi: https://doi.org/10.1016/j.ijfatigue.2017.01.001.

[39]   A. S. f. Testing and Materials, "ASTM E384: standard test method for microindentation hardness of materials," 2017: ASTM West Conshohocken.

[40]   M.-W. Wu, Z.-K. Huang, C.-F. Tseng, and K.-S. Hwang, "Microstructures, mechanical properties, and fracture behaviors of metal-injection molded 17-4PH stainless steel," *Metals and Materials International,* vol. 21, no. 3, pp. 531-537, 2015, doi: https://doi.org/10.1007/s12540-015-4369-y.

[41]   A. Kudzal *et al.*, "Effect of scan pattern on the microstructure and mechanical properties of Powder Bed Fusion additive manufactured 17-4 stainless steel," *Materials & Design,* vol. 133, pp. 205-215, 2017, doi: https://doi.org/10.1016/j.matdes.2017.07.047.

[42]   S. Yin and D. Li, "Effects of prior cold work on corrosion and corrosive wear of copper in HNO3 and NaCl solutions," *Materials Science and Engineering: A,* vol. 394, no. 1-2, pp. 266-276, 2005, doi: https://doi.org/10.1016/j.msea.2004.11.054.

[43]   C. Guo, R. Hu, and F. Chen, "Microstructure and performances for 15-5 PH stainless steel fabricated through the wire-arc additive manufacturing technology," *Materials Technology,* vol. 36, no. 14, pp. 831-842, 2021, doi: https://doi.org/10.1080/10667857.2020.1800296.

[44]   T. Zhou *et al.*, "Microstructure control during deposition and post-treatment to optimize mechanical properties of wire-arc additively manufactured 17-4 PH stainless steel," *Additive Manufacturing,* vol. 58, p. 103047, 2022, doi: https://doi.org/10.1016/j.addma.2022.103047.

[45]   H. Inoue, T. Koseki, S. Ohkita, and M. Fuji, "Formation mechanism of vermicular and lacy ferrite in austenitic stainless steel weld metals," *Science and Technology of Welding and Joining,* vol. 5, no. 6, pp. 385-396, 2000, doi: https://doi.org/10.1179/136217100101538452.

[46]   N. Suutala, "Effect of solidification conditions on the solidification mode in austenitic stainless steels," *Metallurgical Transactions A,* vol. 14, no. 1, pp. 191-197, 1983, doi: https://doi.org/10.1007/BF02651615.

[47]   L. Chen *et al.*, "The Corrosion Behavior of 17-4 Stainless Steel in a Stainless Steel-Carbon Steel Galvanic Couple," *Int. J. Electrochem. Sci,* vol. 12, pp. 9445-9455, 2017, doi: https://doi.org/10.20964/2017.10.40.

[48]   S. Roy *et al.*, "Investigating the effect of different shielding gas mixtures on microstructure and mechanical properties of 410 stainless steel fabricated via large scale additive manufacturing," *Additive Manufacturing,* vol. 38, p. 101821, 2021, doi: https://doi.org/10.1016/j.addma.2020.101821.

[49]   P. Long, D. Wen, J. Min, Z. Zheng, J. Li, and Y. Liu, "Microstructure evolution and mechanical properties of a wire-arc additive manufactured austenitic stainless steel: Effect of processing parameter," *Materials,* vol. 14, no. 7, p. 1681, 2021, doi: https://doi.org/10.3390/ma14071681.

[50]   A. Eghlimi, M. Shamanian, M. Eskandarian, A. Zabolian, M. Nezakat, and J. A. Szpunar, "Evaluation of microstructure and texture across the welded interface of super duplex stainless steel and high strength low alloy steel," *Surface and Coatings Technology,* vol. 264, pp. 150-162, 2015, doi: https://doi.org/10.1016/j.surfcoat.2014.12.060.

[51]   Y. Chao, T.-S. Lui, and L. Chen, "Influence of Creq/Nieq ratio on solidification structures and tensile properties of strip cast austenitic stainless steels," *International Journal of Cast Metals Research,* vol. 9, no. 3, pp. 175-181, 1996, doi: https://doi.org/10.1080/13640461.1996.11819658.

[52]   D. Shaffer, "Role of Retained Austenite in Mechanical Response of Additively Manufactured 17-4 PH Stainless Steel," 2020, doi: https://etda.libraries.psu.edu/catalog/18266djs6031.

[53]   H. Kitahara, R. Ueji, N. Tsuji, and Y. Minamino, "Crystallographic features of lath martensite in low-carbon steel," *Acta materialia,* vol. 54, no. 5, pp. 1279-1288, 2006, doi: https://doi.org/10.1016/j.actamat.2005.11.001.

[54]   I. Vysotskiy, S. Malopheyev, I. Zuiko, S. Mironov, and R. Kaibyshev, "Crystallographic aspects of 17–4 PH martensitic steel produced by laser-powder bed fusion," *Materials Characterization,* vol. 194, p. 112405, 2022, doi: https://doi.org/10.1016/j.matchar.2022.112405.

[55]   P. Krakhmalev, I. Yadroitsava, G. Fredriksson, and I. Yadroitsev, "In situ heat treatment in selective laser melted martensitic AISI 420 stainless steels," *Materials & Design,* vol. 87, pp. 380-385, 2015, doi: https://doi.org/10.1016/j.matdes.2015.08.045.

[56]   O. D. Sherby, J. Wadsworth, D. R. Lesuer, and C. K. Syn, "Revisiting the structure of martensite in iron-carbon steels," *Materials transactions,* vol. 49, no. 9, pp. 2016-2027, 2008, doi: https://doi.org/10.2320/matertrans.MRA2007338.

[57]   J.-Y. Park and Y.-S. Park, "The effects of heat-treatment parameters on corrosion resistance and phase transformations of 14Cr–3Mo martensitic stainless steel," *Materials Science and Engineering: A,* vol. 449, pp. 1131-1134, 2007, doi: https://doi.org/10.1016/j.msea.2006.03.134.

[58]   T. LeBrun, T. Nakamoto, K. Horikawa, and H. Kobayashi, "Effect of retained austenite on subsequent thermal processing and resultant mechanical properties of selective laser melted 17–4 PH stainless steel," *Materials & Design,* vol. 81, pp. 44-53, 2015, doi: https://doi.org/10.1016/j.matdes.2015.05.026.

[59] A. V. Nemani, M. Ghaffari, S. Salahi, J. Lunde, and A. Nasiri, "Effect of interpass temperature on the formation of retained austenite in a wire arc additive manufactured ER420 martensitic stainless steel," *Materials Chemistry and Physics,* vol. 266, p. 124555, 2021, doi: https://doi.org/10.1016/j.matchemphys.2021.124555.

[60] F. Deng, G. Yang, S. Zhou, B. Wu, L. Qin, and J. Zheng, "Effect of heat treatment on microstructural heterogeneity and mechanical properties of maraging steel fabricated by wire arc additive manufacturing using 4% nitrogen shielding gas," *Materials Characterization,* vol. 191, p. 112160, 2022, doi: https://doi.org/10.1016/j.matchar.2022.112160.

[61] J. M. Park *et al.*, "Effect of heat treatment on microstructural heterogeneity and mechanical properties of 1% C-CoCrFeMnNi alloy fabricated by selective laser melting," *Additive Manufacturing,* vol. 47, p. 102283, 2021, doi: https://doi.org/10.1016/j.addma.2021.102283.

[62] N. Sridharan, M. W. Noakes, A. Nycz, L. J. Love, R. R. Dehoff, and S. S. Babu, "On the toughness scatter in low alloy C-Mn steel samples fabricated using wire arc additive manufacturing," *Materials Science and Engineering: A,* vol. 713, pp. 18-27, 2018, doi: https://doi.org/10.1016/j.msea.2017.11.101.

[63] Z. Wang, T. A. Palmer, and A. M. Beese, "Effect of processing parameters on microstructure and tensile properties of austenitic stainless steel 304L made by directed energy deposition additive manufacturing," *Acta Materialia,* vol. 110, pp. 226-235, 2016, doi: https://doi.org/10.1016/j.actamat.2016.03.019.

[64] S. Suryakumar, K. Karunakaran, U. Chandrasekhar, and M. Somashekara, "A study of the mechanical properties of objects built through weld-deposition," *Proceedings of the Institution of Mechanical Engineers, Part B: Journal of Engineering Manufacture,* vol. 227, no. 8, pp. 1138-1147, 2013, doi: https://doi.org/10.1177/0954405413482122.

[65] M. Rafieazad, M. Ghaffari, A. Vahedi Nemani, and A. Nasiri, "Microstructural evolution and mechanical properties of a low-carbon low-alloy steel produced by wire arc additive manufacturing," *The International Journal of Advanced Manufacturing Technology,* vol. 105, pp. 2121-2134, 2019, doi: https://doi.org/10.1007/s00170-019-04393-8.

[66] M. Ghaffari, A. Vahedi Nemani, M. Rafieazad, and A. Nasiri, "Effect of solidification defects and HAZ softening on the anisotropic mechanical properties of a wire arc additive-manufactured low-carbon low-alloy steel part," *Jom,* vol. 71, pp. 4215-4224, 2019, doi: https://doi.org/10.1007/s11837-019-03773-5.

[67] S. Pasebani, M. Ghayoor, S. Badwe, H. Irrinki, and S. V. Atre, "Effects of atomizing media and post processing on mechanical properties of 17-4 PH stainless steel manufactured via selective laser melting," *Additive Manufacturing,* vol. 22, pp. 127-137, 2018, doi: https://doi.org/10.1016/j.addma.2018.05.011.

[68] M. Soleimani, A. Kalhor, and H. Mirzadeh, "Transformation-induced plasticity (TRIP) in advanced steels: a review," *Materials Science and Engineering: A,* vol. 795, p. 140023, 2020, doi: https://doi.org/10.1016/j.msea.2020.140023.

[69] H. Eskandari, H. Lashgari, L. Ye, M. Eizadjou, and H. Wang, "Microstructural characterization and mechanical properties of additively manufactured 17–4PH stainless steel," *Materials Today Communications,* vol. 30, p. 103075, 2022, doi: https://doi.org/10.1016/j.mtcomm.2021.103075.

[70]   Y. Sun, R. J. Hebert, and M. Aindow, "Effect of heat treatments on microstructural evolution of additively manufactured and wrought 17-4PH stainless steel," *Materials & Design,* vol. 156, pp. 429-440, 2018, doi: https://doi.org/10.1016/j.matdes.2018.07.015.

[71]   M. Jamalkhani *et al.*, "Deciphering microstructure-defect-property relationships of vacuum-sintered binder jetted fine 316 L austenitic stainless steel powder," *Additive Manufacturing,* vol. 59, p. 103133, 2022, doi: https://doi.org/10.1016/j.addma.2022.103133.